applied sciences

Article

Chaotic Characteristic Analysis of Spillway Radial Gate Vibration under Discharge Excitation

Yangliang Lu, Yakun Liu *, Di Zhang, Ze Cao and Xuemin Fu

Faculty of Infrastructure Engineering, Dalian University of Technology, Dalian 116024, China; slgclyl@163.com (Y.L.); di.zhang@dlut.edu.cn (D.Z.); caoze@dlut.edu.cn (Z.C.); fuoliver@yeah.net (X.F.)
* Correspondence: liuyakun@dlut.edu.cn

Abstract: This paper aims to assess the nonlinear vibration of a radial gate induced by flood discharge; the measured acceleration response data of a spillway radial gate are analyzed using the chaos theory. The results show that the vibration responses of the gate at three opening heights present clear chaotic characteristics, and the chaotic characteristics of the lower main beam point are greater than other points. Moreover, the y-direction (vertical) correlation dimensions of the three measuring points on the supporting arm are larger than those of the x-direction (axial) and z-direction (lateral). The vertical vibration of the supporting arm is more complex and presents more uncertainties, which should be paid attention to in the literature. Under three different gate opening heights, the maximum Lyapunov exponent of each measuring point ranges from 0.0246 to 0.0681. In addition, the flow fluctuation load is the main excitation source of the gate vibration chaotic characteristics.

Keywords: spillway radial gate; supporting arm; fluid-induced vibration; chaotic characteristics; the maximum Lyapunov exponent

check for updates

Citation: Lu, Y.; Liu, Y.; Zhang, D.; Cao, Z.; Fu, X. Chaotic Characteristic Analysis of Spillway Radial Gate Vibration under Discharge Excitation. *Appl. Sci.* **2024**, *14*, 99. https://doi.org/10.3390/app14010099

Academic Editor: Angelo Luongo

Received: 24 November 2023
Revised: 16 December 2023
Accepted: 17 December 2023
Published: 21 December 2023

1. Introduction

A spillway radial gate (SRG) is frequently used as the working gate for reservoir surface spillways owing to the advantages of its small opening and closingforce, good flow pattern, and easy operation. Therefore, its safe operation is of great significance to the whole hydropower station. However, the SRG is affected by the fluctuating loads of high-speed-flow water in the processes of opening and discharging, resulting in different modes of vibration [1]. Non-linear vibration refers to the motion that cannot be described by linear differential equations. For the gate vibration system, when the SRG vibrates under a discharge excitation condition, the supporting arm can create a dynamic unstable region due to the parametric vibration that is strongly non-linear, which can cause chaos. While assembled by welding and bolt connections [2], the vibrations weaken these junctions, which can finally lead to the failure of gate structures. As a result, further investigations into the characteristics of the vibration of SRGs are necessary to avoid these issues.

To date, many scholars have investigated the fluid-induced vibration (FIV) of SRGs through prototype tests [3], numerical structural calculations [4,5], hydroelastic modeling experiments [6], and principle analyses [7,8]. The analyses showed that the supporting arms were the weakest component of the SRG, which could finally lead to the failure of the gate. On 17 July 1995, the rotation vibration around the supporting hinge of the No. 3 SRG of the Folsom dam in the United States and the low-frequency panel bending vibration were superimposed [9], which induced the strong self-excited vibration of the gate and led to the instability of the supporting arm. Furthermore, on 2 July 1967, the SRG of the Wachi dam in Japan was damaged owing to the out-of-plane bucking instability of the supporting arms [10]. Gate vibrations are often caused by forced, self-excited, and parametric vibrations occurring at the same time in practical engineering [11].

According to the above-mentioned works, the theory of the stability analysis of supporting arms is gradually developing; nevertheless, the complexity of their vibrations have not been analyzed. Jiang et al. [12] used the improved variational mode decomposition (IVMD) technique to conduct a multi-scale chaotic analysis of pipeline vibration responses. Luo et al. [13] collected the time series of the fluctuating pressures in a slit-type energy dissipater of the discharge flow and analyzed the chaotic characteristics of the fluctuating pressure. Luo et al. [14] analyzed the chaotic characteristics of the flow-induced vibration response of the plate gate. However, the method of the hydroelastic test that they adopted could be somewhat different from the actual operation of the gate. Yang et al. [15] used the chaos theory to analyze the prototype test data of the supporting arm during the flood discharge. Both studies adopted the five-point cubic smoothing method to reduce the noise in the data, which can lead to the loss of critical vibration characteristics. On the other hand, the chaotic characteristics of the main beams of the SRG still remain unknown, and the causes of the chaotic phenomena in the gate vibration system are not clear. Hence, it is essential to thoroughly investigate the chaotic characteristics of SRGs.

In this paper, the chaos theory is introduced to process the vibration time series of the supporting arm and main beams of an SRG, and the saturation correlation dimension and maximum Lyapunov exponent are used to quantitatively reverse analyze the chaotic characteristics of gate vibrations. On this basis, we highlight the vibration excitation source of the SRG. This work provides theoretical solutions for avoiding the operation of the gate under complex and small opening conditions in practical engineering, and also increases the use value of the measured data.

2. Methodology

The chaotic characteristics can be identified using both qualitative and quantitative methods, while the qualitative analysis is limited to identify the existence of chaos. Quantitative analysis methods can reflect the degree of complexity of response vibrations under different conditions through the comparison of parameter values. Two quantitative analysis methods, the saturation correlation dimension method and the maximum Lyapunov exponent, are widely used. Through the reconstruction of phase space, the characteristic value of the chaotic system was obtained. On this basis, we judged whether the time series exhibited chaotic characteristics, analyzed the complexity of the time series, and then studied the complexity of the vibration of the SRG under the discharge excitation condition.

2.1. Reconstruction of Phase Space

2.1.1. Time Delay

The time series of the acceleration data of the gate, x_t ($t = 1, 2, 3, \ldots, N$), is assigned to a new m-dimensional state vector, Y_n ($n = 1, 2, 3, \ldots, N - (m-1)\tau$), based on the appropriate delay-coordinate method:

$$\boldsymbol{Y}_n = \left\{ x_n, x_{n+\tau}, x_{n+2\tau}, L, x_{n+(m-1)\tau} \right\} \tag{1}$$

where τ is the time delay and represents the multiple sampling time intervals for the measured data, while m represents the embedding dimension.

By choosing a reasonable embedding dimension, m, and time delay, τ, an equivalent phase space can be reconstructed and the attractor of the prime dynamic system can be obtained. In present work, the average mutual information (AMI) [16] method with a strong anti-noise ability was used to determine the time delay, τ. And the AMI function $I(\tau)$ is defined as:

$$I(\tau) = \sum_{i,i+\tau} P(x_i, x_{i+\tau}) lnP(x_i, x_{i+\tau}) - \sum_{i} P(x_i) lnP(x_i) - \sum_{i+\tau} P(x_{i+\tau}) lnP(x_{i+\tau}) \tag{2}$$

where $P(x_i)$ and $P(x_{i+\tau})$ are the independent probability densities of x_i and $x_{i+\tau}$, respectively, and $P(x_i, x_{i+\tau})$ is the combined probability densities of x_i and $x_{i+\tau}$. The optimal time delay was determined as corresponding to the first minimum of $I(\tau)$.

2.1.2. Embedding Dimension

The averaged false nearest neighbors (AFN)-CAO method [17] was employed to determine the optimal embedding dimension, which improved the false nearest neighbors method and presented considerable advantages in dealing with time series containing noise. The CAO method is defined as:

$$E_1(m) = E(m)/[E(m+1)] \tag{3}$$

$$E(m) = \frac{1}{N - m\tau} \sum_{i=1}^{N-m\tau} a(i,m) \tag{4}$$

$$a(i,m) = \frac{\left\| \mathbf{Y}_i(m+1) - \mathbf{Y}_{n(i,m)}(m+1) \right\|}{\left\| \mathbf{Y}_i(m) - \mathbf{Y}_{n(i,m)}(m) \right\|}, i = 1,2,3,L,(N - m\tau) \tag{5}$$

where $E_1(m)$ is the rate of variation of $E(m)$; $E(m)$ is the average of $a(I, m)$; and $Y_{n(i,m)}(m)$ denotes the nearest vector of $Y_i(m)$ in an m-dimensional space.

Assume that:

$$E_2(m) = E^*(m+1)/[E^*(m)] \tag{6}$$

$$E^*(m) = \frac{1}{N - m\tau} \sum_{i=1}^{N-m\tau} \left| x_{i+m\tau} - x_{n(i,m)+m\tau} \right| \tag{7}$$

where $E_2(m)$ is the level of change in $E^*(m)$ and $E^*(m)$ is the level of trace change in $E_2(m)$. For a completely stochastic time series, $E_2(m)$ is always near 1, regardless of the values of τ and m. However, for a chaotic time series, $E_2(m)$ increases and approaches 1 with the increase in m. And the m value, when $E_2(m)$ is equal to 1 and does not change, was perceived as the minimum embedding dimension. $E_1(m)$ and $E_2(m)$ were calculated to determine the embedding dimension, m, at the same time.

2.2. Identification of Chaotic Characteristics

2.2.1. Correlation Dimension

The saturation correlation dimension is a dimension extracted from chaotic attractors, which describes the degree of chaos of nonlinear dynamical systems represented by time series. For an m-dimensional space, its correlation function is defined as:

$$C(r) = \lim_{M\to\infty} \frac{2}{M(M-1)} \sum_{1\le i\le j\le M} H(r - \left\| \mathbf{Y}_i - \mathbf{Y}_j \right\|) \tag{8}$$

where $C(r)$ is the correlation function; r is the vector point; M is the phase-point numbers, and $\left\| \mathbf{Y}_i - \mathbf{Y}_j \right\|$ is the distance between two points, i and j, in the phase space.

When the time series has a chaotic attractor feature, for a positive value, r, the relation between $C(r)$ and r is expressed as:

$$C(r) \propto \alpha r^{D_2} \tag{9}$$

where α is the constant and D_2 represents the correlation dimension, which can be calculated by the slope of the *lnC*(r)~*lnr* curve:

$$D_2 = \lim_{r\to 0} \frac{lnC(r)}{lnr} \tag{10}$$

Due to the existence of noise in the measured data, the initial embedding dimensions were usually specified at low numbers and gradually increased. In each embedding dimension, the part of the ln$C(r)$~ln$r$ curve that presented a constant slope was employed for fitting using the least squares method. The slope of this part of the ln$C(r)$~ln$r$ curve increased with the increase in the embedding dimension and eventually reached the saturation value, which was the correlation dimension.

2.2.2. Maximum Lyapunov Exponent

The Lyapunov exponent was used to identify the chaotic characteristics of the system according to the diffusion of the phase trajectory. The positive Lyapunov exponent is a distinct indicator of chaos, representing directions that support the attractor. In contrast, the negative Lyapunov exponent corresponds to the contraction direction. We set the Lyapunov exponent as λ_1. If λ_1 is positive, it can be concluded that there is a chaotic component in the system and its magnitude reflects the degree of chaos. Rosenstein et al. [18] proposed a method for calculating λ_1. The basic steps included selecting appropriate τ and m values for the phase-space reconstruction, determining the nearest neighbor values, $\boldsymbol{Y}_{\hat{i}}$, of each point, $\boldsymbol{Y}_i$, in the phase space, and limiting the temporal separation using:

$$d_i(0) = \min_{\hat{i}} \left\| \boldsymbol{Y}_i - \boldsymbol{Y}_{\hat{i}} \right\|, \left(\left| i - \hat{i} \right| \right) > p \tag{11}$$

where p is the average period of the time series, i is the vector in space, and $\hat{i}$ is the vector of the nearest neighbor, $\boldsymbol{Y}_{\hat{i}}$, of the second vector.

We defined the distance between the adjacent point, j, and discrete time steps as:

$$d_i(j) = \boldsymbol{Y}_{i+j} - \boldsymbol{Y}_{\hat{i}+j} \tag{12}$$

where $j = 0, 1, 2, 3, \ldots, min(M - i, M - i)$.

For each value of j, the $\ln d_i(j)$ average can be derived as follows:

$$y(j) = \frac{1}{q\Delta t} \sum_{i=1}^{q} \ln d_i(j) \tag{13}$$

where q is the number of non-zero $\ln d_i(j)$. The least squares method was used to create a regression line, the slope of which was λ_1.

2.3. Principle of the CEEMDAN Algorithm

The complete ensemble empirical mode decomposition with adaptive noise algorithm (CEEMDAN) is an adaptive data analysis method for dealing with nonstationary and nonlinear signals [19]. It can effectively solve the problems of mode mixing and false intrinsic mode function (IMF) generated by the empirical mode decomposition (EMD) and can overcome the residual problem of ensemble empirical mode decompositions (EEMDs). Therefore, the reconstruction error is approximately 0 with shorter average times, and the calculation efficiency is higher. The CEEMDAN decomposition process is described as follows:

Step 1: Add white noise, $\varepsilon_0 n_i(t)$, to the original signal, $x(t)$. ε_0 is the amplitude coefficient of the white noise added for the first time. Then, the ith signal can be expressed as $x_i(t) = x(t) + \varepsilon_0 n_i(t)$. For each $x_i(t)$ that experiences the EMD, the first-order component, imf_{i1}, and residual, $r_{i1}(t)$, of each signal were obtained, which were $imf_1 = \frac{1}{n}\sum_{i=1}^{n} imf_{i1}$ and $r_1(t) = x(t) - imf_1$, respectively.

Step 2: Define the operator, $E(\cdot)$, as the jth component after using the EMD, add white noise to it, and then decompose it to obtain the second component:

$$imf_2 = \frac{1}{n} \sum_{i=1}^{n} E_1\{r_1(t) + \varepsilon_1 E_1[n_i(t)]\} \tag{14}$$

Then the k residual signal is:

$$r_k(t) = r_{k-1}(t) - imf_k \tag{15}$$

Step 3: Compute the component of the $(k+1)$th mode:

$$imf_{k+1} = \frac{1}{n}\sum_{i=1}^{n} E_1\{r_1(t) + \varepsilon_k E_k[n_i(t)]\} \tag{16}$$

Step 4: Repeat steps 2 and 3 until the signal cannot be decomposed and the operation terminates. Total K components are obtained and the final residual signal is:

$$r(t) = x(t) - \sum_{i=1}^{K} imf_i \tag{17}$$

Finally, the original signal can be represented as:

$$x(t) = \sum_{i=1}^{K} imf_i + r(t) \tag{18}$$

3. SRG Analysis of the Prototype Test Data

3.1. Project Introduction

A hydropower station on Yalong River is located in southwest China. There are five surface outlets in the spillway of the surface hole of the gravity dam section. Each outlet is equipped with an emersed radial gate with a radius of 21.00 m and width of 15.00 m. The material used for the SRG is Q345C steel. The SRG is arranged on the top of the WES weir, and the downstream is connected to the combination of a Y flaring gate pier, stepped spillway, and stilling basin to dissipate energy. Due to the large slope of the downstream channel of the gate, the flow pattern behind the gate is a typical free outflow, as shown in Figure 1. The working conditions of the dynamic prototype tests are detailed in Table 1.

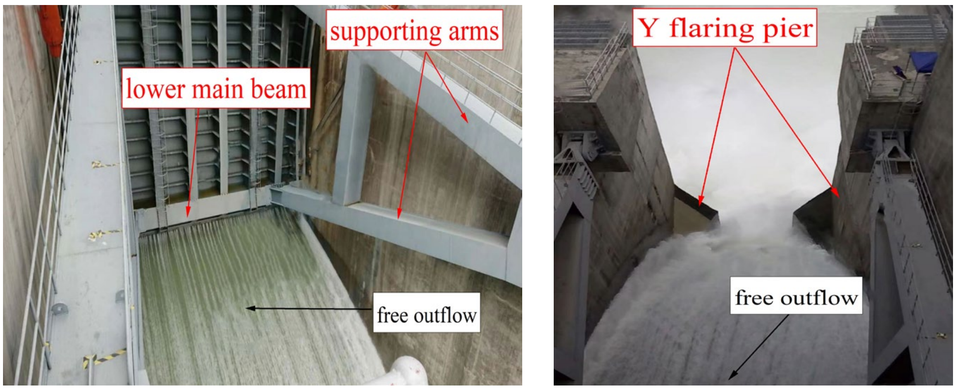

Figure 1. Flow pattern after the opening of the SRG (No. 3#).

Table 1. Three working conditions of the dynamic prototype tests.

Condition	Absolute Opening Height h (m)	Gate Opening Ratio $e = h/H$ (%)	Discharge (m^3/s)	Velocity of Bottom Edge (m/s)
1	3.50	18	606	15.78
2	2.40	12	405	15.17
3	1.00	5	183	16.89

In order to fully track the vibration characteristics of the sensitive area (main beam and supporting arm) under hydrodynamic loads, three triaxial acceleration sensors were arranged on the top-left arm of the SRG (No. 3#) to measure the axial, vertical, and lateral vibrations of the supporting arm. Similarly, two triaxial acceleration sensors were arranged on the upper and lower main beams of the gate, and the schematic diagram of the measurement points is shown in Figure 2. The triaxial vibration acceleration sensor had a sensitivity of 1000 Mv/g with a frequency range of 0.1~2 KHz and a resolution of 0.00002 g. The sampling frequency and duration of each opening gate were 200 Hz and 120 s, respectively. It has to be emphasized that, for the three triaxial acceleration sensors on the gate leaf, the *x*-direction represented the radial direction of the gate leaf and the *y*- and *z*-directions denoted the tangential and lateral directions of the gate leaf, respectively. Moreover, for the sensors on the supporting arm, the *x*-direction denoted the axial direction of the supporting arm, the *y*-direction denoted the direction that was perpendicular to the supporting arm, and the *z*-direction represented the lateral direction. Note that the aforementioned sensor directions are defined in the local coordinate systems, and the directions in the global coordinate system may change with different gate opening values. For the sensors installed on the radial gate, the lateral direction (*z*-direction points on the gate leaf and supporting arm) always remained horizontal and did not change in the global coordinate system; the *y*- and *z*-directions were dependent on the gate opening heights and were inconsistent under different working conditions.

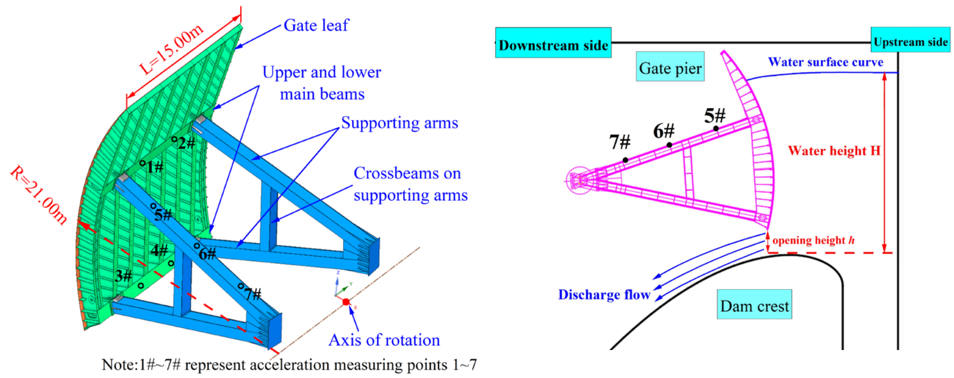

(**a**) (**b**)

Figure 2. Diagram of the SRG: (**a**) layout of SRG (No. 3#) acceleration measuring points; (**b**) partial opening diagram of the SRG.

Figure 3 shows the root mean square (RMS) of the vibration acceleration of the measuring points on the supporting arm under three working conditions. Point 5# is located at the front end of the upper-left supporting arm, close to the upper main beam on the gate; point 6# is located in the middle of the upper-left supporting arm; and point 7# is located at the back end of the upper-left supporting arm, which is close to the supporting hinge. In Figure 3, we can clearly observe that point 7 in the *y*-direction under condition 1 is the highest. The *Y*-direction denotes the direction that is perpendicular to the supporting arm. Firstly, according to the relevant prototype observation results, the vertical vibration of the supporting arm is obviously higher than that of the axial- and lateral-direction vibrations. Moreover, the position of point 7 is close to the end of the supporting arm, which is close to the joint of the fixed and movable supporting hinges. There is a gap in the connecting part of the fixed and movable hinges, which may increase the vibration intensity. In addition, it can be seen that the vibration of each measuring point on the supporting arm obeys no obvious rule with the change in the opening heights, and it is difficult to draw an intuitive conclusion.

Hydrodynamic loads were the key factors that caused the structural vibrations of the radial gate. When the flow velocity was higher than 5 m/s, the fluctuation and violent turbulence occurred based on the jet flow. Therefore, it was important to determine the velocity field distribution in order to analyze the vibration characteristics of the spillway radial gate, as no comprehensive and continuous flow field information could be obtained due to the limited nature of the prototype test. Numerical simulations that adopted the RNG k-ε turbulent model were performed using Ansys Fluent 2021R1 software to simulate the flow field [20,21], which served as inputs for the subsequent analysis of the gate vibration in this paper. Its grid diagram is shown in Figure 4, with a total grid of 2.94 million; Figure 5 shows the schematic diagram of the open flow pattern. According to the flow field derived from the numerical simulations, the flow pattern after the water flowed out of the bottom edge of the gate was relatively smooth, which presented a typical free outflow pattern. The flow velocity distribution of the bottom edge under different gate opening heights is shown in Figure 6. Note that the 2D profile presented in Figure 6 is located on the x–z plane on the center line of the spillway, as shown in Figure 5. It can be seen that the high-flow-velocity zone (flow velocity higher than 5 m/s) under working condition 1 presents the greatest range of effect, followed by working condition 2 and finally working condition 3 that has the least range of effect. When comparing the maximum flow velocity of the bottom edge, we derived the formula of condition 3 > condition 1 > condition 2, where no qualitative rule could be determined. Hence, it was necessary to analyze the chaotic characteristics of the gate's nonlinear vibration response.

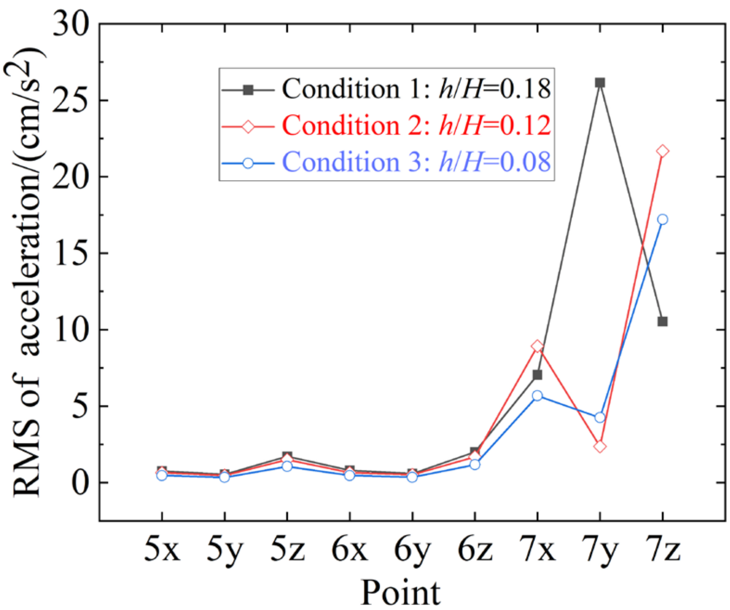

Figure 3. RMS of the vibration acceleration of measuring points on the supporting arm.

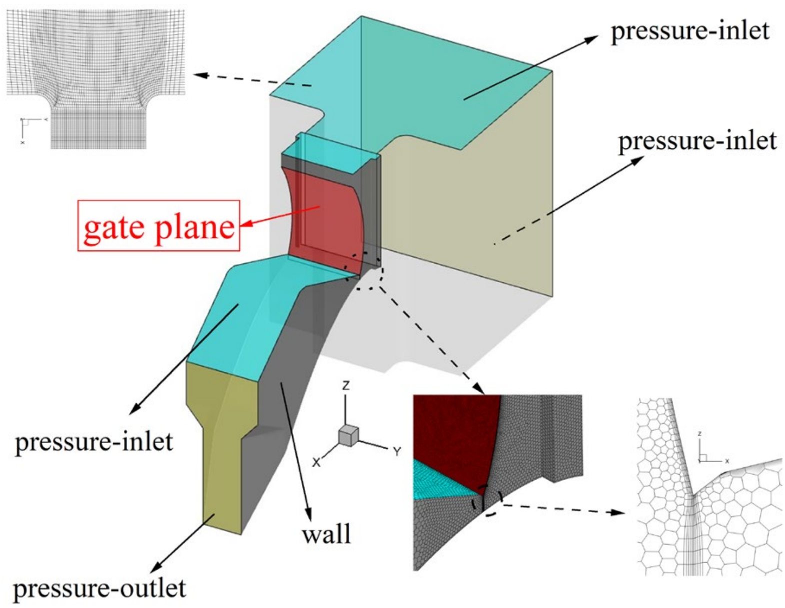

Figure 4. Three-dimensional grid diagram.

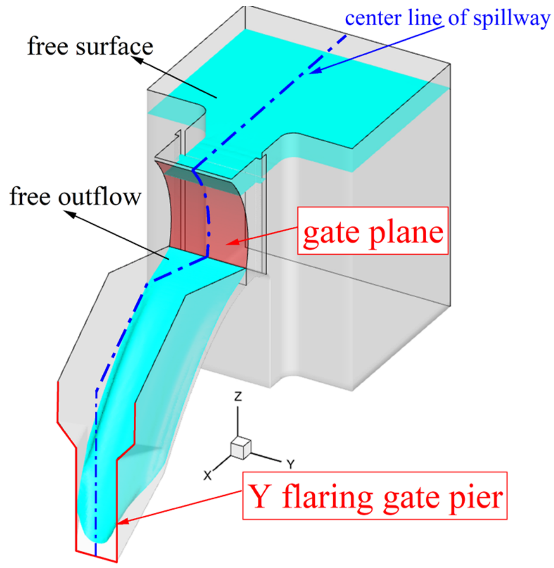

Figure 5. Flow pattern diagram of the discharge flow.

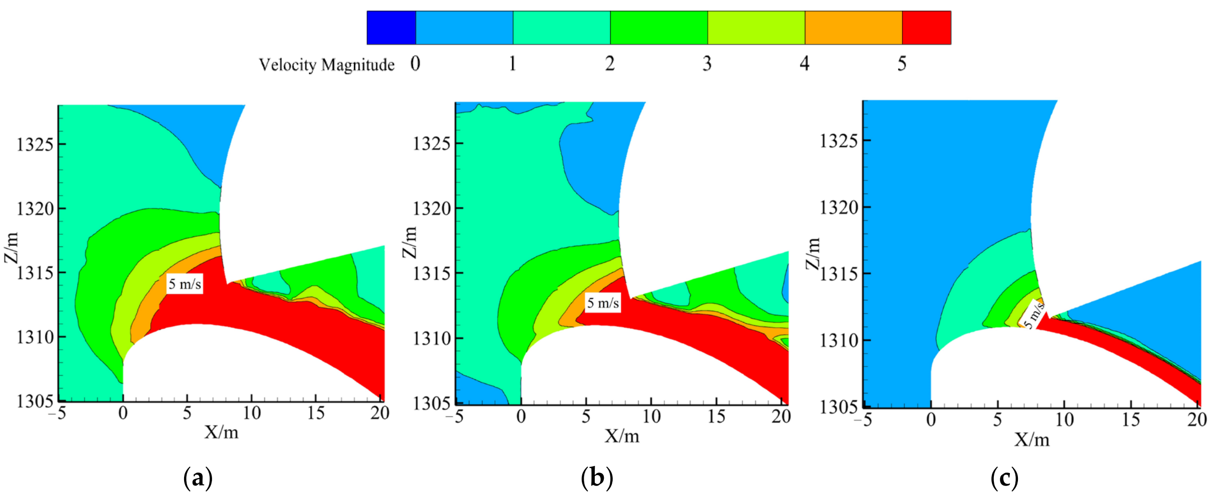

Figure 6. Contours of velocity magnitudes near the bottom edge of SRG under three working conditions: (**a**) condition 1 (h = 3.5 m); (**b**) condition 2 (h = 2.4 m); (**c**) condition 3 (h = 1.0 m).

3.2. Signal Denoising

In the processes of transmission and acquisition, the vibration signal of the discharge structure is easily affected by high-frequency white noise and low-frequency water flow, which is usually represented by a low SNR and non-stationary random signal [22]. In addition, the presence of noise affected the results derived from the chaos theory. Therefore, it was necessary to reduce the noise level before analyzing the chaotic characteristics of the data.

After the original signals were decomposed by CEEMDAN to obtain the IMF components, the intensity of the noise in each IMF component could be determined by calculating the multi-scale permutation entropy (MPE) value. This measured the randomness of the time variance values of the signals at different scales [23], with a magnitude approaching 1 indicating relatively high randomness and non-stationarity values. The MPE threshold was set to 0.6 [24] in this work, and the MPE values of IMF components higher than or equal to 0.6 were regarded as noisy components and needed further filtering out by the wavelet threshold denoising (WTD) method.

The principle of the WTD method is that the wavelet coefficients generated by the signal through the wavelet transform contains important information regarding the signal.

The real signal possessed coefficients with relatively high magnitudes, while the noise signal presented relatively low coefficients. By setting a reasonable threshold for the wavelet coefficient, the wavelet coefficient lower than the threshold was perceived as noise and set to 0 to eliminate the effect of noise. The steps performed were as follows:

(1) Select the appropriate wavelet basis and the number of decomposition layers to conduct the wavelet decomposition of noisy signals;
(2) Select the appropriate threshold method for the threshold processing of wavelet coefficients at each decomposition scale;
(3) Reconstruct the wavelet coefficient to complete the noise reduction process.

The common threshold function is divided into soft and hard threshold functions [25, 26], which are given in Equations (19) and (20), respectively:

$$W_{j,k} = \begin{cases} sgn(w_{j,k}(\left|w_{j,k}\right| - \lambda)), \left|w_{j,k}\right| \geq \lambda \\ 0, \left|w_{j,k}\right| < \lambda \end{cases} \tag{19}$$

$$W_{j,k} = \begin{cases} w_{j,k}, \left|w_{j,k}\right| \geq \lambda \\ 0, \left|w_{j,k}\right| < \lambda \end{cases} \tag{20}$$

Here, Equation (19) denotes the soft threshold function and Equation (20) denotes the hard threshold function. $W_{j,k}$ denotes the wavelet decomposition coefficient and $W_{j,k}$ is the wavelet coefficient after decomposition. λ is the threshold value.

However, the discontinuity of the hard threshold function at the threshold point and the constant error of the soft threshold function still affected the denoising to some extent. Therefore, in this paper, a new threshold function was introduced to overcome these shortcomings. It combines the characteristics of the soft and hard threshold values, which is expressed as the following equation:

$$W_{j,k} = \begin{cases} sgn(w_{j,k}) \times \left| \left|w_{j,k}\right| - \frac{\lambda}{\sqrt[\beta]{\left|w_{j,k}\right|^{\beta} - |\lambda|^{\beta} + 1}} \times \frac{1}{e^{\sqrt[\alpha]{|w_{j,k}| - |\lambda|}}} \right|, \left|w_{j,k}\right| \geq \lambda \\ 0, \left|w_{j,k}\right| < \lambda \end{cases} \tag{21}$$

The equation above was continuous at the threshold point, so it could overcome the discontinuity of the hard threshold function at the threshold and meet the condition of an odd function. A comparison of different thresholding functions is shown in Figure 7.

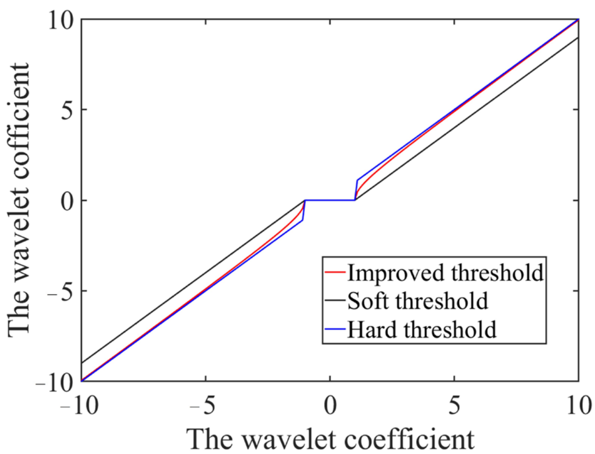

Figure 7. Comparison of different thresholding functions.

Whether it was a hard, soft, or improved threshold function, the choice of threshold, λ, is very important. A fixed threshold is widely used in engineering, and the effect of noise reduction is obvious when there is a lot of noise. The natural frequency of an ambient vibration of the gate was relatively low, and the fixed threshold criterion was more effective for denoising purposes. At present, the selection of λ is adopted for the fixed threshold (sqtwolog) mainly based on the following formula:

$$\lambda = \sqrt{2lnN} \tag{22}$$

where N is the length of the signal sequence.

The power values of the effective and noise signals were unknown and the signal-to-noise ratio could not be used to judge the noise reduction effect in the actual project. Therefore, this paper introduced the denoise signal-to-noise ratio (dnSNR) to judge the noise reduction quality [27]. The calculation formula is as follows:

$$dnSNR = 10lg(P_s/P_g) \tag{23}$$

where Ps is the power of the noise signal and Pg is the power of the denoised signal. The lower the $dnSNR$ value, the more significant the noise reduction effect.

The combined denoising method of CEEMDAN-MPE-IWTD was used to process the original signal. The realization flowchart of the CEEMDAN-MPE-IWTD method is shown in Figure 8. For the measuring points on the main beams, point 3# in the x-direction is located on the lower main beam, which is closest to the high-speed flow at the bottom edge of the gate, and the y-direction on the lower main beam indicates the direction of the downstream flow. Therefore, point 3# has certain representativeness. The noise reduction effect at point 3# in the x-direction is shown in Figure 9. Figure 9b shows the normalized power spectrum (NPS) curves, where the normalization method is both two power spectral density curves divided by the maximum power spectral density of the original signal. At the same time, the noise reduction effects of the soft, hard, and improved wavelet thresholds were compared, as shown in Table 2. It can be observed from the table that the noise reduction error ratio of the CEEMDAN-MPE-IWTD algorithm is the smallest, indicating that the algorithm has the best noise reduction effect.

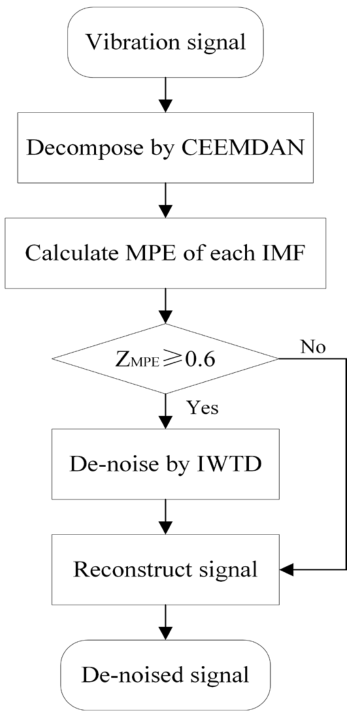

Figure 8. Flowchart of the CEEMDAN-MPE-IWTD method. Note: Z_{MPE} denotes the multi-scale permutation entropy (MPE) of each intrinsic mode function (IMF) component.

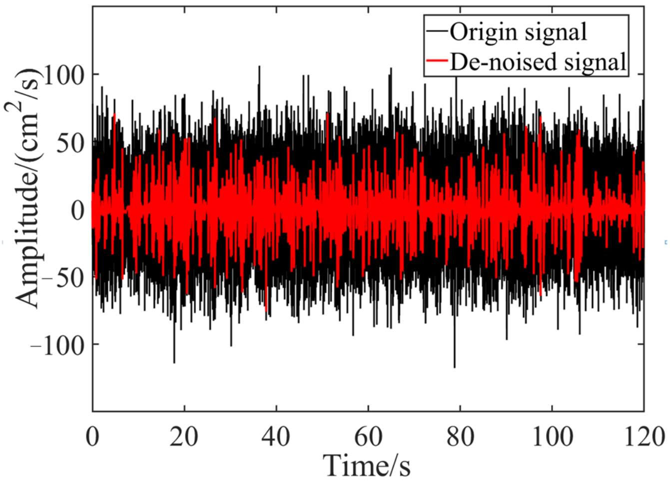

(**a**)

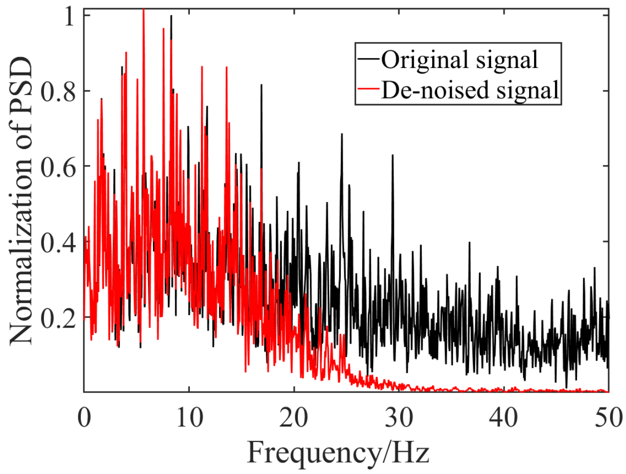

(**b**)

Figure 9. Comparison of vibration acceleration values before and after noise reduction stages at measuring point 3# in the x-direction: (**a**) time history curves and (**b**) normalized power spectrums (NPSs).

Table 2. Comparison results of the *dnSNR* values.

Method	*dnSNR*
CEEMDAN-MPE-HWTD	1.95
CEEMDAN-MPE-SWTD	1.85
CEEMDAN-MPE-IWTD	1.83

Note: the CEEMDAN-MPE-HWTD method represents a combined denoising method based on the complete ensemble empirical mode decomposition with adaptive noise (CEEMDAN), multi-scale permutation entropy (MPE), and hard wavelet threshold denoising (HWTD) methods. Moreover, SWTD denotes soft wavelet threshold denoising, and IWTD denotes improved wavelet threshold denoising.

4. Results and Discussion

4.1. Phase-Space Reconstruction of the Vibration Acceleration Data

As can be seen from the layout of t*he* gate vibration acceleration points in Figure 2, points 2# and 4# are at symmetrical locations with respect to points 1# and 3#, respectively. Therefore, this study focused on analyzing the vibration acceleration characteristics in the three directions of measuring point 1# on the upper main beam, point 3# on the lower main beam, and points 5#, 6#, and 7# on the upper supporting arm.

The denoised signal was reconstructed in the phase space and the AMI method was used to calculate the optimal time delay, τ. Figure 10 shows the AMI calculation diagram of point 3# in the x-direction (the radial direction of the gate leaf) under condition 1, and the results derived from this method are summarized in Table 3. After determining the optimal time delay, the optimal embedding dimension was selected using the AFN method. The variations in E_1 and E_2 of the point 3# x-directional data with m are shown in Figure 11. According to Figure 11a, the E_2 curve before the noise reduction always fluctuates at a small range of around 1 for any m value, indicating that the random noise sequence is mixed into the time series. As shown in Figure 11b, the apparent deviation of the E_2 curve after the noise reduction from 1 exists at a relatively low m value, and finally approaches 1 as m increases, indicating that E_2 is obviously related to m. This method can be used to determine whether the time series exhibits chaotic characteristics. When the value of the E_1 function no longer changes significantly with the embedding dimension, and the value of the E_2 function approaches 1, the corresponding m value is the optimal embedding dimension.

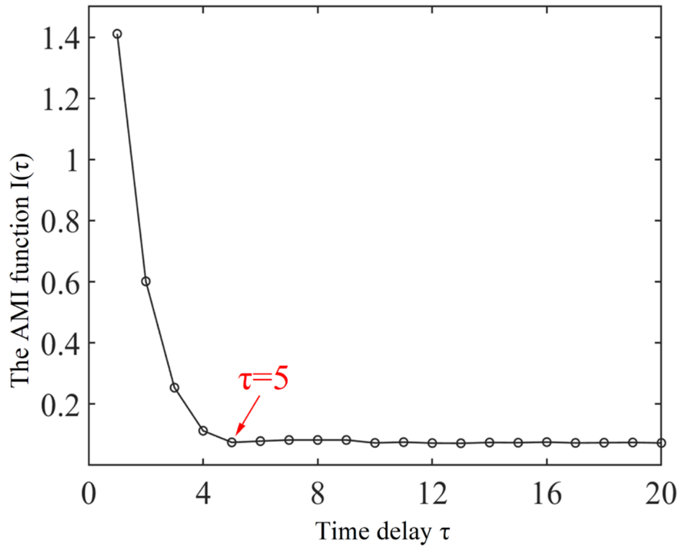

Figure 10. τ calculation of point 3# in the x-direction (the radial direction of the gate leaf) under condition 1.

Table 3. τ and m values of vibration acceleration time series of measuring points.

Condition	Point	1			3			5			6			7		
		x	y	z	x	y	z	x	y	z	x	y	z	x	y	z
1	τ	5	5	6	5	8	5	4	5	5	4	4	5	4	4	4
	m	21	21	20	20	21	22	22	25	22	24	24	25	22	22	24
2	τ	4	7	7	5	5	6	4	5	8	4	4	5	4	4	4
	m	21	20	20	20	22	22	22	21	23	21	19	19	22	22	24
3	τ	5	7	8	5	5	5	5	5	6	5	5	5	5	5	4
	m	22	19	19	21	20	20	22	22	21	22	21	21	20	21	22

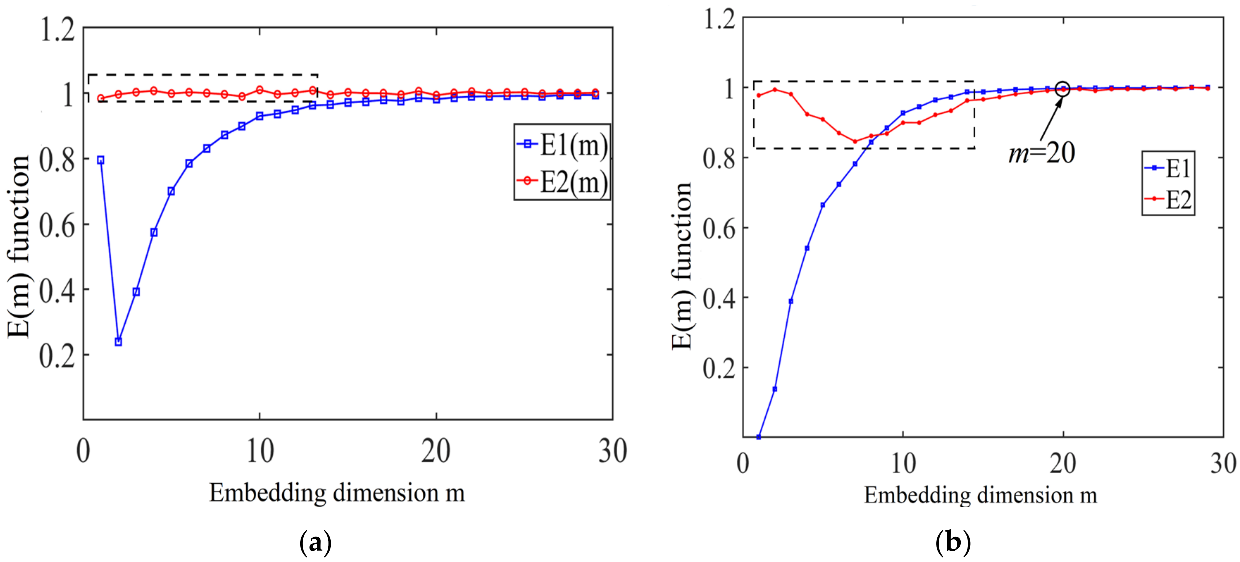

Figure 11. Point 3# x-direction vibration acceleration embedding dimension before (**a**) and after (**b**) noise reduction stages under condition 1.

It can be seen from Table 3 that the time delay, τ, is generally in the range of 4~8; it reaches 8 near or on the main beam. The time delay values of measuring points 6# and 7# on the supporting arm are relatively short with magnitudes between 4~5, indicating that the vibration complexity near the supporting hinge is relatively low. The overall value of the optimal embedding dimension, m, is between 19 and 25. The embedding dimension, m, at opening height h = 3.5 m is slightly larger than that at the opening sizes h = 2.4 m and 1.0 m. The FIV complexity of the gate at a relatively large opening is greater than that at a small opening.

4.2. Chaotic Characteristic Analysis

4.2.1. Correlation Dimension Analysis

The G-P algorithm [28] was selected to calculate the saturation correlation dimension. According to the optimal time delay, τ, the embedding dimension gradually increased from m = 2 to 30, and the relationship between $C(r)$ and r was calculated according to Equation (9); then, the double logarithmic relation curve of different m values was obtained.

For the measuring points on the supporting arm, the RMS amplitude of the vibration acceleration of point 7# was higher than those of points 5# and 6#. Taking the results from the point 7 z-direction as an example, Figure 12 shows that the double logarithmic relation curve with an arrow indicates the increased m value from 2 to 30. Select the section of the curve with an approximately linear variation and take its slope as the correlation dimension under the corresponding embedding dimension. The correlation dimension in Figure 13 increases with the increase in the embedding dimension till it reaches the saturated correlation dimension, D_2. Figure 13 shows the relationship between D_2 and m of the acceleration time series. According to this step, the law of the correlation dimension variation of each measuring point under three working conditions was calculated, as shown in Figure 14.

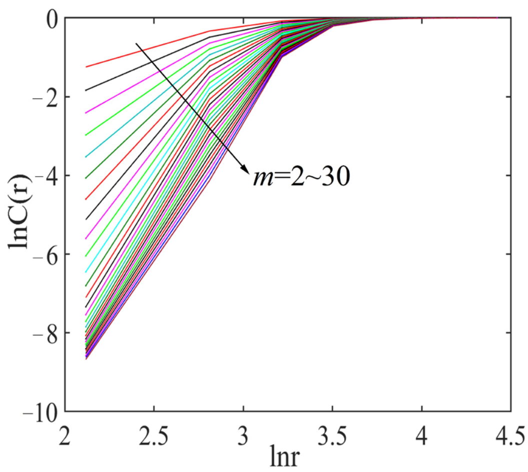

Figure 12. ln$C(r)$ versus ln$r$ plots for the vibration series of point 7 in the z-direction.

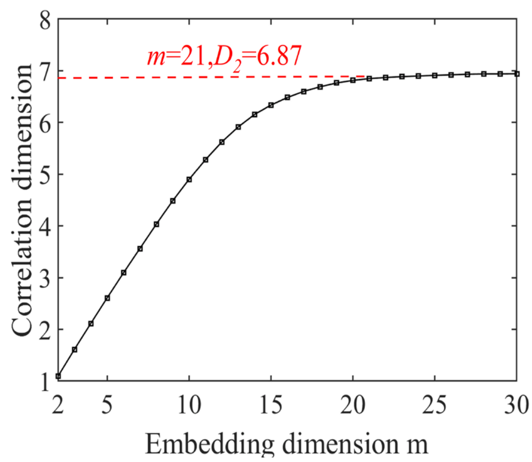

Figure 13. Relationship between D_2 and m at point 7 in the z-direction.

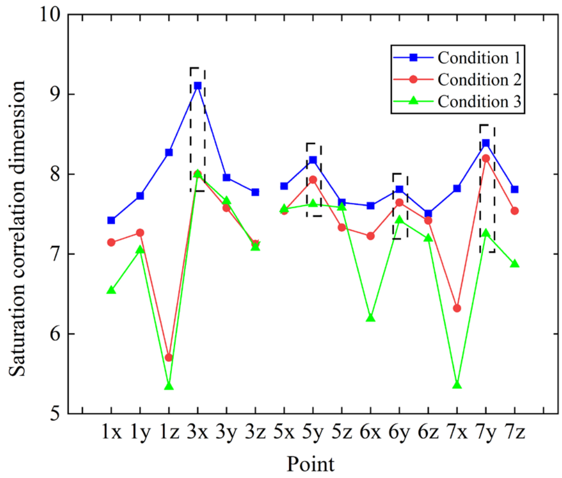

Figure 14. Saturation correlation dimension of 5 points in different directions under three working conditions.

It can be concluded from Figure 14 that:

(1) The results show that the correlation dimension reaches the saturation value of the embedding dimension, which agrees well with the calculated results attained by the AFN method, indicating that the acceleration signal after the noise reduction stage can better reflect the chaotic characteristics of the SRG.

(2) Overall, the correlation dimension varies from 5.2561 to 9.1092. The correlation dimension of point 1 in the z-direction under conditions 1 and 3 and point 7 in the x-direction present the lowest magnitudes, and the remaining points are concentrated in the range of 6.1916~9.1092. All of the correlation dimensions are fractional numbers, which indicates that the FIV response in each direction on the SRG exhibit chaotic and fractal characteristics.

(3) At the same measuring points, the correlation dimension, D_2, of each measuring point under condition 1 is larger than those under conditions 2 and 3, indicating that the uncertainty of the gate vibration increases when the opening is large.

(4) The saturation correlation dimension of point 3 presents the highest magnitude of the correlation dimension in the direction along the x-axis, indicating that the lower main beam has the most complex vibration.

(5) The y-direction (vertical) correlation dimensions of the three measuring points on the supporting arm are large and the x-direction (axial) measurement point on the supporting arm is obviously small, indicating that the axial direction of the supporting arm presents a lower-dimensional chaotic attractor. The complexity and nonlinear law of the vibration process of the axial direction of the supporting arm can be determined by using fewer independent control variables.

The reference [8] results show that, when the dynamic instability zone-induced parametric vibration of the supporting arm is generated under the action of the fluctuating load, the out-of-plane vibration of the supporting arm has a remarkable influence on the dynamic instability of the SRG. Therefore, more attention should be paid to the vertical (y-direction) vibration of the supporting arm when monitoring the gate vibration.

4.2.2. Maximum Lyapunov Exponent Analysis

In order to verify the above-mentioned analysis results, the maximum Lyapunov exponent, λ_1, was chosen to further analyze the chaotic characteristics of the SRG with different opening sizes. Using the above-selected optimal embedding parameters, the maximum Lyapunov exponent, λ_1, was calculated using small datasets. Figure 15 presents a calculation diagram of measuring point 7 in the z-direction. It can be seen that the separation factor remains stable following the linear growth activity. The least squares fitting of the line close to growing segment presents the slope as the maximum Lyapunov index, λ_1. The reconstructed attractor is bounded and the latter half is stable and invariant. Thus, the separation factor, $y(j)$, does not exceed the attractor range. The distribution of λ_1 at different measuring points under three working conditions is shown in Figure 16.

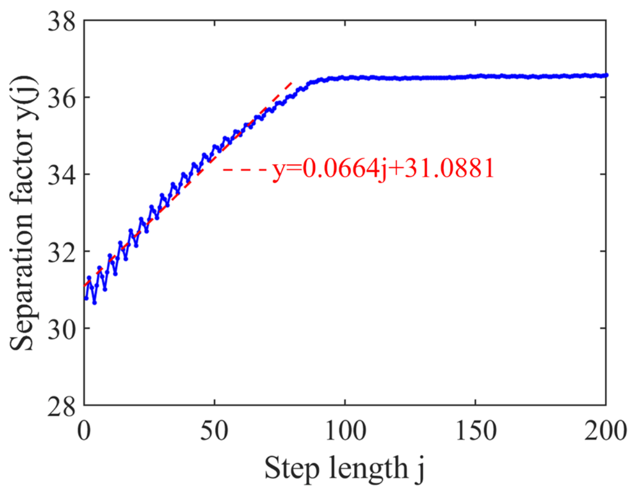

Figure 15. The maximum Lyapunov exponent, λ_1, of point 7 in the z-direction.

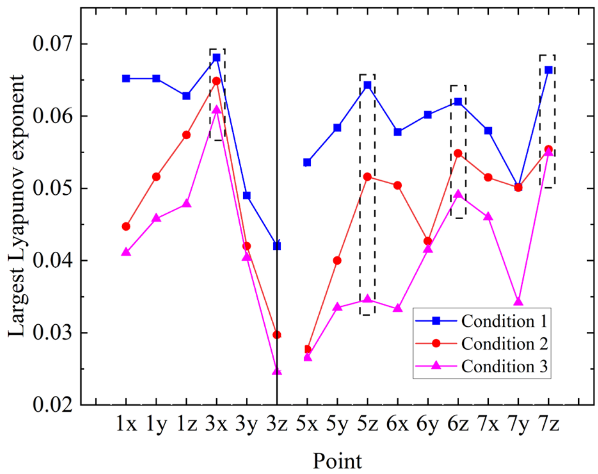

Figure 16. The maximum Lyapunov exponent of 5 points in different directions under three working conditions.

As shown in Figure 16:

(1) Under three working conditions, the maximum Lyapunov index value of each measuring point ranges from 0.0246 to 0.0681, which is greater than 0. It shows that the vibration responses of the main beams and supporting arm have obvious chaotic characteristics during the water discharge process.

(2) In general, except for a few measuring points, the λ_1 value of each measuring point under working condition 1 is the highest. The chaotic characteristics of the gate vibration gradually weakens with the decrease in the gate opening sizes, which is consistent with the chaotic characteristics derived from the saturation correlation dimension.

(3) The λ_1 value of point 3 in the x-direction on the lower main beam presents the highest magnitude, followed by its results along the y- and z-directions. The upper main beam obeys no obvious rule. The λ_1 value of point 3 along the x-direction is obviously higher than that of point 3 along the x-direction, indicating that the lower main beam is more affected by the flow pattern under the gate bottom edge and exhibits chaotic characteristics.

(4) The lateral vibration, λ_1, values of the three measuring points on the supporting arm are greater than the radial and vertical values on the supporting arm.

4.3. Discussion

It can be seen from Figure 9b that high-frequency components appear in the NPS of the original signal, which may result from the high-order local vibration highlighted by the gate and high-frequency white noise collected by the sensor. The vibration energy values of the high-frequency components are low and the NPS amplitude is less than 0.5, which is not the overall vibration value of the gate. Similarly, Jiang et. al [12] supposed that the vibration sources for a pumping station pipe mainly included the low-frequency flow-water fluctuation caused by flow water and the blade frequency, rotation frequency, and frequency doubling caused by the unit's operation. The low-frequency fluctuating load of flow water was the main cause of the chaotic characteristics of the pumping station pipeline. However, the vibration source was relatively simple when the gate was opened, that is, the low-frequency dynamic water load acting on the gate panel. In order to further clarify the vibration excitation characteristics that caused the gate to exhibit chaotic characteristics, the CEEMDAN decomposition results of the vibration signal in the point 3# x-direction on the lower main beam mentioned above were used as an example. Three components, IMF1, IMF2, and IMF3–14, were compared. As previously mentioned, Figure 9 shows the comparison of the vibration acceleration values before and after the noise reduction stages at point 3# in the x-direction. Figure 17 shows the time variances and normalized power spectral density curves of the three components.

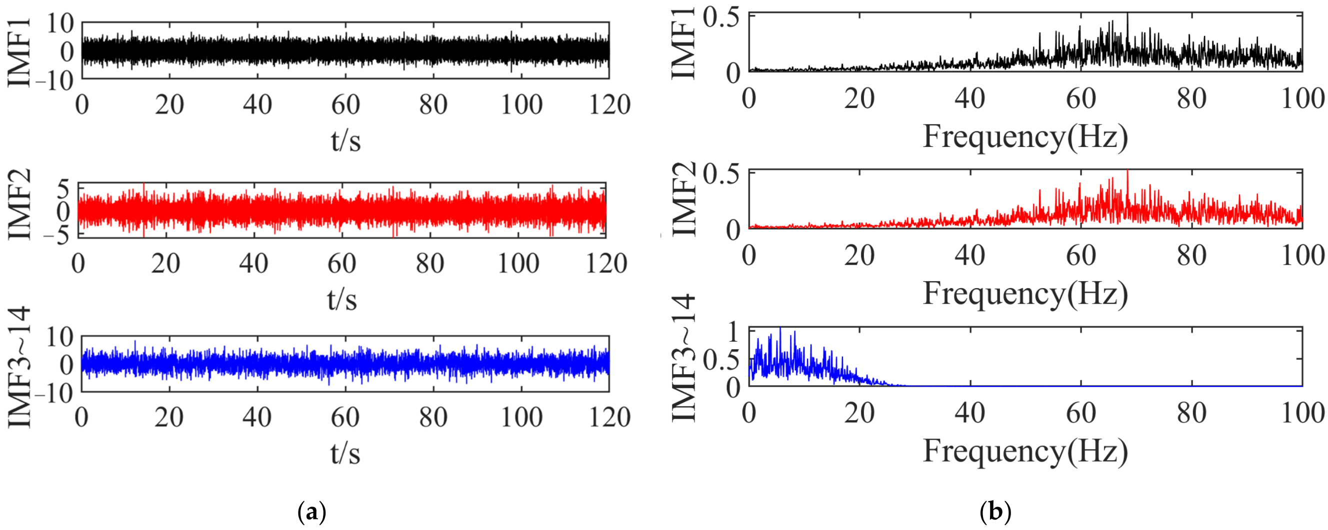

Figure 17. Time and frequency domain diagrams of point 3# in the x-direction for different IMF components: (**a**) time histories of each IMF component and (**b**) NPS of each IMF component.

It can be seen from Figure 17b that the vibration energy is concentrated between 40 and 100 Hz in acceleration components IMF1 and IMF2, respectively, of point 3# along the x-direction, and the NPS is less than 0.5. The main energy values of the IMF3–14 components are mainly concentrated between 0.1 and 20 Hz. According to statistics [8], 93% of the gate flow-water fluctuation main frequency variations were below 20 Hz, and few exceeded 20 Hz. Due to the limitations of the observation conditions, although the fluctuating pressure sensors were not installed on the gate panel, it could be inferred from the existing studies that the IMF3~14 component was mainly the low-frequency forced vibration component of the gate induced by the flow-water fluctuation. Therefore, the analyses of the chaotic characteristics of IMF1, IMF2, and IMF3–14 representing different components can further clarify the exhibition of chaotic gate characteristics.

As shown in Figure 18, the maximum Lyapunov exponents, λ_1, of IMF1 and IMF2 are 0.0192 and 0.0348, while the maximum Lyapunov exponent, λ_1, of IMF3–14 is 0.0744. The maximum Lyapunov exponents of IMF1 and IMF2 are 0.0681 after the IWTD was denoised and combined with the remaining components. If the vibration excitation components (IMF1 and IMF2) with weak chaotic characteristics were removed, the maximum Lyapunov exponents, λ_1, of IMF3–14 increased from 0.0681 to 0.0744, and the chaotic characteristics were more obvious. The above-mentioned results show that the forced vibration of the gate is chaotic due to the fluctuating load acting on the gate panel.

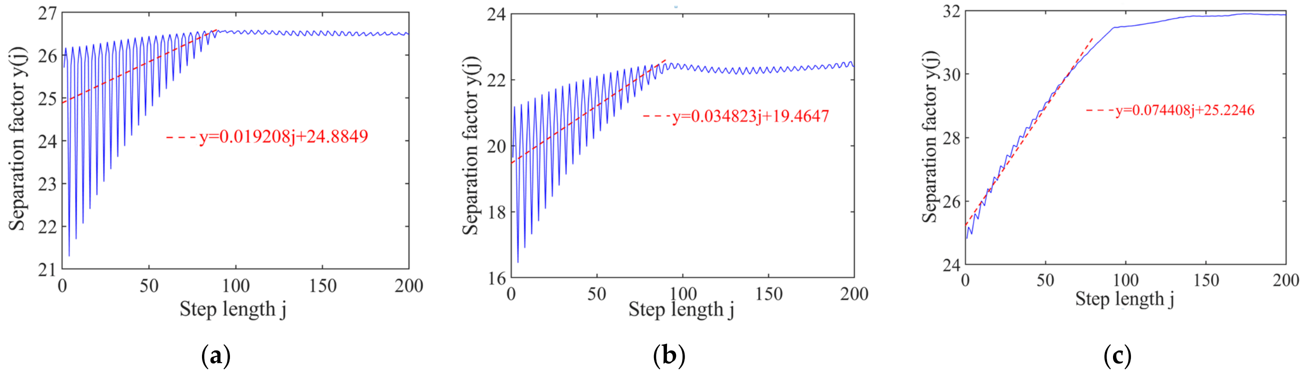

Figure 18. λ_1 values for different IMF components of point 3# in the x-direction: (**a**) λ_1 of IMF1; (**b**) λ_1 of IMF2; (**c**) λ_1 of IMF3–14.

5. Conclusions

In this paper, an improved noise reduction method was adopted to process the vibration signal of an SRG, and the vibration characteristics of both the main beam and supporting arm were studied from the perspective of chaos. The following conclusions were drawn:

(1) The FIV values in three directions of five total measuring points on the SRG exhibited chaotic and fractal characteristics. The y-direction (vertical) correlation dimension of the three measuring points on the supporting arm was greater. Therefore, more attention should be paid to the vertical vibration of the supporting arm when monitoring the gate's vibration.

(2) For three opening heights, the maximum Lyapunov exponent of each measuring point ranged from 0.0246 to 0.0681. The lateral direction, λ_1, values of the three measuring points on the supporting arm were greater than those along the radial and vertical directions of the supporting arm.

(3) The chaotic characteristics of the SRG mainly resulted from the fluctuating pressure exerted by the high-speed flow water on the gate.

At present, with the development of sustainable hydropower energy generation, more SRGs need to be operated at small opening heights for the safe and intelligent regulation of reservoirs. Hence, sensitive openings should be avoided according to the chaotic characteristic parameter that is evident at small gate openings.

Author Contributions: Conceptualization, Y.L. (Yangliang Lu) and Y.L. (Yakun Liu); methodology, Y.L. (Yangliang Lu), Y.L. (Yakun Liu), D.Z. and Z.C.; software, Y.L. (Yangliang Lu) and X.F.; validation, Y.L. (Yangliang Lu), Y.L. (Yakun Liu) and X.F.; formal analysis, Y.L. (Yangliang Lu), Y.L. (Yakun Liu), D.Z. and Z.C.; software, Y.L. (Yangliang Lu) and X.F.; writing—original draft preparation, Y.L. (Yangliang Lu); writing—review and editing, Y.L. (Yangliang Lu) and X.F.; funding acquisition, Y.L. (Yakun Liu) and D.Z. All authors have read and agreed to the published version of the manuscript.

Funding: This research was supported financially by the National Natural Science Foundation of China (grant No. 52179060; 51909024).

Institutional Review Board Statement: Not applicable.

Informed Consent Statement: Not applicable.

Data Availability Statement: The data provided in this study are available from the corresponding author. The data are not publicly available due to privacy.

Conflicts of Interest: The authors declare no conflict of interest.

References

1. Liu, Y.K.; Ni, H.G.; Ye, Z.Q.; Liu, Y.L. Analysis of flow-induced vibration of hydraulic radial gate. *J. Dalian Univ. Technol.* **2005**, *5*, 730–734. (In Chinese)
2. Zhang, X.; Lou, S.; Chen, L.; Wang, Z.; Zhang, F. Study on Analysis Principle of Spatial System Method for a Hydraulic Steel Gate. *Sustainability* **2022**, *14*, 4804. [CrossRef]
3. Lian, J.; Chen, L.; Ma, B.; Liang, C. Analysis of the Cause and Mechanism of Hydraulic Gate Vibration during Flood Discharging from the Perspective of Structural Dynamics. *Appl. Sci.* **2020**, *10*, 629. [CrossRef]
4. Lee, S.O.; Seong, H.; Kang, J.W. Flow-induced vibration of a radial gate at various opening heights. *Eng. Appl. Comput. Fluid Mech.* **2018**, *12*, 567–583. [CrossRef]
5. Zhang, B.; Jing, X. Theoretical analysis and simulation calculation of hydrodynamic pressure pulsation effect and flow induced vibration response of radial gate structure. *Sci. Rep.* **2022**, *12*, 21932. [CrossRef]
6. Anami, K.; Knisely, C.W.; Todd, R.V.; Ishii, N.; Oku, T. Vibration Tests with a 1/13-Scaled 3-D Model of the Folsom Dam Tainter-gate and its Prediction by Theory. In Proceedings of the 6th Symposium on Fluid-Structure Interactions, Aeroelasticity and Flow-Induced Vibration and Noise, Vancouver, BC, Canada, 23–27 July 2006; pp. 703–710.
7. Xu, C.; Wang, Z. New insights into dynamic instability regions of spillway radial gate owing to fluid-induced parametric oscillation. *Nonlinear Dyn.* **2022**, *111*, 4053–4070. [CrossRef]
8. Xu, C.; Wang, Z.; Zhang, H.; Li, H.; Li, D. Investigation on mode-coupling parametric vibrations and instability of spillway radial gates under hydrodynamic excitation. *Appl. Math. Model.* **2022**, *106*, 715–741. [CrossRef]
9. Anami, K.; Ishii, N. Flow-Induced Dynamic Instability Closely Related to Folsom Dam Tainter-Gate Failure in California. In Proceedings of the 7th International Conference on Flow-Induced Vibration (FIV 2000), Luzern, Switzerland, 19–22 June 2022; pp. 205–212.
10. Anami, K.; Ishii, N.; Knisely, C.W.; Tsuji, T.; Oku, T.; Sato, S. Friction-Maintained Dynamic Stability. In Proceedings of the 10th Biennial International Conference on Vibration Problems (ICOVP), Prague, Czech Republic, 5–8 September 2011; pp. 779–785.
11. Xu, C.; Liu, J.; Zhao, C.; Liu, F.; Wang, Z. Dynamic failures of water controlling radial gates of hydro-power plants: Advancements and future perspectives. *Eng. Fail. Anal.* **2023**, *148*, 107168. [CrossRef]
12. Jiang, L.; Ma, Z.; Zhang, J.; Khan, M.Y.A.; Cheng, M.; Wang, L. Chaotic Characteristic Analysis of Vibration Response of Pumping Station Pipeline Using Improved Variational Mode Decomposition Method. *Appl. Sci.* **2021**, *11*, 8864. [CrossRef]
13. Luo, B.E.; Wang, J.X.; Zhang, Y.Y. Researches on the Chaotic Characteristics of Fluctuating Pressure in Slit-Type Energy Dissipater. *Adv. Mater. Res.* **2014**, *1025–1026*, 1150–1159. [CrossRef]
14. Luo, B.E.; Wang, J.X.; Zhou, J.; Zhang, Y.Y. Research on the Characteristics of Flow-Induced Vibration of Bulkhead Gate Based on Chaotics Theory. *J. Vib. Meas. Diagn.* **2016**, *36*, 187–193+206. (In Chinese) [CrossRef]
15. Yang, J.; Xu, G. Vibration Characteristics of Radial Gate Arm Based on Chaos Theory. *Water Resour. Power* **2020**, *38*, 169–172+200. (In Chinese)
16. Kraskov, A.; Stögbauer, H.; Grassberger, P. Estimating mutual information: Art. no. 066138. *Phys. Rev. E* **2004**, *69*, 066138. [CrossRef] [PubMed]
17. Cao, L.Y. Practical method for determining the minimum embedding dimension of a scalar time series. *Phys. D* **1997**, *110*, 43–50. [CrossRef]
18. Rosenstein, M.T.; Collins, J.J.; De Luca, C.J. A Practical Method for Calculating Largest Lyapunov Exponents from Small Data Sets. *Phys. D-Nonlinear Phenom.* **1993**, *65*, 117–134. [CrossRef]
19. Torres, M.E.; Colominas, M.A.; Schlotthauer, G.; Flandrin, P. A Complete Ensemble Empirical Mode Decomposition with Adaptive Noise. In Proceedings of the IEEE International Conference on Acoustics, Speech, and Signal Processing (ICASSP), Prague, Czech Republic, 22–27 May 2011; pp. 4144–4147.
20. Yang, Z.; Yin, J.; Lu, Y.; Liu, Z.; Yang, H.; Xu, G. Three-Dimensional Flow of a Vortex Drop Shaft Spillway with an Elliptical Tangential Inlet. *Water* **2021**, *13*, 504. [CrossRef]
21. Li, J.Y.; Wang, C.; Wang, Z.Z.; Ren, K.L.; Zhang, Y.L.; Xu, C.; Li, D.F. Numerical Analysis of Flow-Induced Vibration of Deep-Hole Plane Steel Gate in Partial Opening Operation. *Sustainability* **2022**, *14*, 13616. [CrossRef]
22. Li, H.; Wang, G.; Wei, B.; Liu, H.; Huang, W. Improved variational mode decomposition method for vibration signal processing of flood discharge structure. *J. Vib. Control.* **2021**, *28*, 2556–2569. [CrossRef]
23. Wang, G.; Li, H.; Fu, Z.; Huang, W.; Liu, B.; Yao, S. A novel methodology for modal parameter identification of arch dam based on multi-level information fusion. *Mech. Syst. Signal Process.* **2023**, *183*, 109578. [CrossRef]
24. Liu, Z.; Peng, Y. Study on Denoising Method of Vibration Signal Induced by Tunnel Portal Blasting Based on WOA-VMD Algorithm. *Appl. Sci.* **2023**, *13*, 3322. [CrossRef]

25. Azzalini, A.; Farge, M.; Schneider, K. Nonlinear wavelet thresholding: A recursive method to determine the optimal denoising threshold. *Appl. Comput. Harmon. Anal.* **2005**, *18*, 177–185. [CrossRef]
26. Xie, M.; Liu, J.H.; Lu, S. Elastic Wave Denoising in the Case of Bender Elements Type Piezoelectric Transducers. *Sustainability* **2022**, *14*, 12605. [CrossRef]
27. Xu, L.; Cai, D. Application of de-noising method mixed with CEEMDAN and wavelet transform to signal de-noising for fiber optic gyro monitoring system. *Water Resources Hydropower Eng.* **2018**, *49*, 87–95. (In Chinese) [CrossRef]
28. Grassberger, P.; Procaccia, I. Measuring the strangeness of strange attractors. *Phys. D* **1983**, *9*, 189–208. [CrossRef]